Catalysis Science & Technology

ROYAL SOCIETY OF CHEMISTRY

PAPER

Published on 03 August 2026

Cite this: DOI: 10.1039/d6cy00469e

Tuning Cu–Zn–Mg catalysts by flame spray pyrolysis for CO_2-to-methanol synthesis

Lorena Baumgarten, [ab] Edward Kusumowidagdo,[ab] Linda Klag, [a] Mariam L. Schulte, [ab] Emanuel N. O. A. Bauer, [ab] Thomas A. Zevaco, [b] Justus Just, [c] Erisa Saraçi [ab] and Jan-Dierk Grunwaldt *[ab]

CO_2-hydrogenation is a key route for producing renewable methanol, a carbon-neutral chemical and energy carrier. As this reaction is highly structure-sensitive, many studies have focussed on understanding the structure–activity relationships in typical Cu/ZnO based catalysts. In addition to ZnO, MgO has been identified as a basic support that can further promote methanol synthesis activity. Flame spray pyrolysis (FSP) is a versatile synthesis technique that enables to prepare nanocrystallne materials and to tune the interaction and structure in multicompoenent systems by varying the flame spray configurations. In this study, we explore the direct interaction of Cu, ZnO and MgO through variations of single and double flame FSP configurations for Cu/MgO/ZnO model catalysts. The catalysts were characterized by ICP-OES, XRD, STEM, N_2 physisorption, N_2O titration, Raman spectroscopy, H_2-TPR and *operando* XAS. The results elucidate that varition of the flames in FSP allows tuning the metal–metal oxide interactions, as reflected by differences in reduction behavior, surface area, phase composition, crystallite size and catalytic performance during CO_2 hydrogenation to methanol. Notably, the single-flame catalyst exhibited the highest methanol space–time yield despite its lower surface area and larger crystallites, indicating a particularly strong metal–metal oxide interaction. In contrast, the double-flame catalyst, with Zn introduced separately from Cu–Mg, showed enhanced Zn reducibility and improved Cu stability under transient H_2-dropout conditions. These findings highlight the potential of FSP to tailor metal–support interactions and suggest that separate Zn deposition can enhance catalyst stability while maintaining high methanol productivity.

Received 10th April 2026,
Accepted 19th July 2026

DOI: 10.1039/d6cy00469e

rsc.li/catalysis

1. Introduction

Transforming renewable energy into chemical energy by electrolysis of water and combining it with a carbon source such as CO_2 is summarized under the term Power-to-X.[1] The resulting products can serve as replacement for chemicals derived from fossil resources.[2] An important molecule in this aspect is methanol, which is produced at about 100 million tons annually and the demand is expected to rise further in future.[3] Currently, almost all methanol is produced from fossil-derived syngas (*e.g.* from coal/natural gas, CO and H_2 with 2–5% CO_2) *via* net CO hydrogenation (eqn (1)) at conditions of 50–100 bar and 200–350 °C.[4] The catalyst that has been industrially widely applied and the focus of research for decades is $Cu/ZnO/Al_2O_3$ (CZA).[5] The shift from fossil-based syngas and CO heavy feed towards a CO_2-based feedstock introduces new challenges for the established catalytic systems. CO_2 hydrogenation to methanol (eqn (2)) is thermodynamically less favored and produces one mole water per mole methanol, amplifying deactivation of the CZA catalyst due to sintering of ZnO.[6] The competing reaction is the reverse water–gas shift reaction, which leads to CO and additional water formation (eqn (3)).

The importance of promoters for enhancing Cu-based catalysts during methanol synthesis is well established. In particular, ZnO and also MgO are recognized as highly effective promoters that significantly increase the catalytic activity of Cu towards methanol formation. While ZnO has long been applied industrially, MgO has emerged as an alternative promoter and in both cases, the promoting effect is typically attributed to a synergistic metal–metal oxide interaction, increasing the number of active Cu sites.

[a] *Institute for Chemical Technology and Polymer Chemistry, Karlsruhe Institute of Technology, Engesserstr. 20, 76131 Karlsruhe, Germany.*
E-mail: grunwaldt@kit.edu
[b] *Institute of Catalysis Research and Technology, Karlsruhe Institute of Technology, Hermann-von-Helmholtz Platz 1, 76344 Eggenstein-Leopoldshafen, Germany*
[c] *MAX IV Laboratory, Lund University, Fotongatan 2, 22484 Lund, Sweden*

$$CO + 2\ H_2 \rightleftharpoons CH_3OH \quad \Delta H_{298K} = -90.8\ kJ\ mol^{-1} \quad (1)$$

$$CO_2 + 3H_2 \rightleftharpoons CH_3OH + H_2O \quad \Delta H_{298K} = -49.5\ kJ\ mol^{-1} \quad (2)$$

$$CO_2 + H_2 \rightleftharpoons CO + H_2O \quad \Delta H_{298K} = +41.2\ kJ\ mol^{-1} \quad (3)$$

The beneficial role of Zn for the catalytic activity of Cu catalysts during methanol synthesis is undisputed, although the exact nature of the active Zn species remains debated.[7–10] Strong metal–support interactions (SMSI) are commonly discussed as origin of the enhanced activity of Zn promoted Cu catalysts[11–13] while others attribute this effect to a CuZn alloy.[14–16] Regardless of the exact species, the promoting effect originates from a synergetic relationship between Cu and Zn, where a high interfacial area is essential.[17] ZnO plays both an electronic promoter role[18] and a structural role as spacer and support for the active Cu particles.[19,20] Similarly, MgO as basic support has been identified as an effective promoter for methanol synthesis over Cu catalysts. Nielsen *et al.*[21] reported that Cu/MgO exhibits a higher methanol formation rate during CO hydrogenation than unsupported Cu, Cu/Al_2O_3 and $Cu/ZnO/Al_2O_3$. They attributed this promoting effect to a synergistic metal–support interaction, where CO reacts with basic OH groups at the MgO surface, resulting in a key reaction intermediate.[21] Moreover, lattice oxygen in MgO is activated by charge transfer from Cu.[22] Liu *et al.*[23] found that the presence of MgO increases turnover rates, decreases the Cu particle size and therefore increases metal–support interfacial area. The promoting roles of ZnO and MgO can also act cooperatively. Pandey *et al.*[24] reported that incorporating MgO in a Cu/ZnO catalyst increases the number of defective sites, enhances activity in CO hydrogenation to methanol and improves the stability compared to Cu/MgO alone. The strongest metal–support interaction was observed for Cu on a mixed ZnO–MgO support, where incorporation of 20% Mg influences particle size, dispersion and surface area; all of which directly affects the catalytic performance.[24] Cu/MgO/ZnO catalyst solve the problem, that detailed insight into metal–metal oxide interactions is hindered partly due to the dominant contribution of bulk ZnO, as pointed out by Dalebout *et al.*[25] X-ray absorption spectroscopy (XAS) is widely used to study these catalysts *in situ* and *operando*, but its bulk sensitivity makes Cu–Zn interface phenomena difficult to isolate. To address this, a model system using co-precipitated Cu/MgO has been utilized, where MgO replaces bulk ZnO.[26] Small amounts of Zn were precisely added onto the catalytic surface by impregnation. This approach suppresses interference from spectator ZnO during *operando* experiments and allows direct investigation of metal–promoter interactions.

In recent years, flame spray pyrolysis (FSP) has emerged as fast and reproducible one-step preparation method for nanostructured catalysts.[27–29] In FSP, a precursor solution is finely sprayed into a high-temperature flame, where it undergoes rapid combustion, solvent evaporation, and precursor decomposition, forming highly supersaturated vapor species.[27] These species nucleate to primary oxide particles, which then grow by coagulation and sintering before being rapidly quenched.[30] The intense flame temperature promotes crystallinity, while the fast-cooling preserves nanoscale particle sizes. In a single-flame configuration, all precursors are mixed within one reaction zone, leading to co-nucleation and early interaction of different metal species, often resulting in strongly agglomerated mixed-oxide particles with intimate interfaces. In contrast, double-flame FSP spatially separates precursor feeds into two intersecting flames; particles form individually in each flame and only collide in the mixing zone, allowing controlled hetero-agglomeration where particle interfaces form later, reducing premature co-sintering and offering greater control over composition and agglomerate structure.[31] This dual-nozzle approach has been successfully employed to engineer complex catalytic systems such as Pt–FeO_x/CeO_2 (ref. 28) and $CoMo/Al_2O_3$ (ref. 29) by precisely managing the contact between active component and support. Variations in flame configuration such as feed rate, precursor and solvents allow for easy tuning of relevant catalysts properties such as surface area, particle size distribution and synergetic effects.[32–36] These aspects make FSP an ideal synthesis method to study catalysts for the structure-sensitive methanol reaction. Recently, multiple research groups have successfully synthesized Cu-based catalysts using the FSP technique.[33,34] Tada *et al.*[33] developed flame-made CuO/ZrO_2 catalysts, varying the CuO particle size while maintaining the size and morphology of ZrO_2. Their findings indicated that catalysts with smaller CuO particles exhibited greater methanol selectivity at a given CO_2 conversion compared to both catalysts with larger CuO particles and commercial $CuO/ZnO/Al_2O_3$. They demonstrated that the two-nozzle FSP method used in this contribution is a promising synthetic procedure for highly active CO_2 hydrogenation catalysts. Similarly, Ahmad *et al.*[34] successfully employed FSP to prepare a $Cu/ZnO/Al_2O_3$ catalyst for the direct synthesis of dimethyl ether from syngas. Their study highlighted several advantageous properties of the catalyst, including a high Cu surface area, effective interaction between Cu, ZnO and Al_2O_3, and the presence of small Cu particles. These characteristics contributed to the catalysts superior activity and product selectivity compared to commercially available catalysts. Furthermore, Zhu *et al.*[35] compared flame-made Cu/ZnO, Cu/CeO_2, and $Cu/ZnO–CeO_2$ catalysts and identified the formation of Zn-decorated Cu sites as explanation for enhanced methanol synthesis. Their work further validated FSP as a promising method for developing multicomponent catalysts for methanol synthesis. Recently, a study by Schulte *et al.*[37] showed that the catalyst particle size of a flame-sprayed $Cu/ZnO/ZrO_2$ catalyst could be tuned by variation of the precursor feed rate. These studies clearly show the potential of FSP as a versatile tool for the development of catalyst with specific morphology and/or composition.

Despite this progress, how the flame-spray pyrolysis (FSP) configuration governs Cu–(Zn,Mg) interfacial proximity and the resulting redox behavior under CO_2-to-methanol conditions remains unresolved. While metal–metal oxide interactions have been demonstrated in FSP-prepared systems, the combined promoting effects of ZnO and MgO on Cu have not yet been systematically studied, despite their known effect of enhancing methanol synthesis. Furthermore, *operando* studies on FSP-derived catalysts are scarce, limiting our understanding of how combustion-induced interactions influence the catalyst properties (such as SMSI) under relevant conditions. This is particularly important because a simultaneous combustion of precursors in a joined flame is expected to promote intimate mixing and strong metal–metal oxide interactions. The degree of such synergistic interaction could strongly influence the catalysts redox behavior and stability under varying conditions.

This stability becomes especially critical under the dynamic, non-steady-state operating conditions of interest to Power-to-X processes, where fluctuations in renewable energy can lead to transient hydrogen supply deficits (H_2-dropouts). During such dropouts in extreme cases, the sudden exposure to an oxidizing, H_2-depleted feed can induce severe structural degradation and metal oxidation.[38–40] Utilizing non-steady-state forcing experiments such as a H_2-dropouts serves as a crucial stress test to uncover hidden dynamic phenomena and evaluate how specific catalyst configurations can buffer the interfacial redox potential and protect the active phase from irreversible deactivation.[38,41]

To address this knowledge gap, we investigated how the flame configuration (single *vs.* double) modulates Cu/MgO/ZnO contact/composite formation, which in turn controls reducibility and redox resilience during operation and H_2-dropout through metal–support interaction, thereby impacting methanol space–time yield (STY). To test this, we first run a brief Zn-loading evaluation (5/10/15%) to identify an optimum, then fixed the Zn content and systematically vary the flame configuration and metal distribution (CuZn–Mg, CuMg–Zn, Cu–MgZn), which resulted in a set of catalyst with distinct local structures and catalytic performance. Comprehensive characterization using ICP-OES, XRD, BET, SEM-EDX, STEM, N_2O chemisorption, Raman spectroscopy and *operando* XAS was used with the aim to correlate composition, morphology and electronic structure with catalytic behavior. This approach is expected to give new insight into how synergetic promoter effects from ZnO and MgO govern Cu-based methanol synthesis from CO_2 under (dynamic) conditions.

2. Experimental

2.1 Catalyst preparation

Cu/MgO/ZnO (CMZ) catalysts were prepared *via* flame spray pyrolysis using either one or two nozzles. Cupric acetate monohydrate (Fluka Chemie AG, >99%), magnesium acetate tetrahydrate (VWR Chemicals) and zinc acetate dihydrate (Fluka Chemie AG, >99%) were dissolved in a 1 : 1 volumetric mixture of methanol (Merck, >99.9%) and acetic acid (Merck, >99%). The three metal precursors were either dissolved as one solution (700 mL) or in two separate solutions (700 mL each), as schematically shown in Fig. S1. A picture of the setup is provided in Fig. S2 in SI. The atomic ratio of the metals was varied between 65% Cu, 25% Mg and 10% Zn; 60% Cu, 25% Mg and 15% Zn or 69% Cu, 26% Mg and 5% Zn. Using an ultrasonic bath for 2 h enabled a complete dissolution of the solid precursors. The precursor solutions were transferred into one or two separate 60 mL syringes, depending on the flame configuration (SF: single flame, DF: double flame). The solution(s) were dosed through one or two nozzle(s) with a feed rate of 5 mL min^{-1} using a syringe pump (Legato 210, KD Scientific). In case of the two-flame configuration, the nozzles were tilted by an angle of 30° towards each other, maintaining a distance of 14 cm between the nozzles. Before dispensing the precursor solution(s), the premixed feed of methane (0.75 L min^{-1}) and oxygen (1.6 L min^{-1}) was ignited. An additional oxygen stream (5 L min^{-1}) was blended for enhanced dispersion of the precursor spray with a backpressure of 3 bar. Each gas flow was regulated using mass flow controllers (Bronkhorst). The obtained powder was collected approximately at a distance of 50 cm to the nozzle on a fiberglass filter (Whatman GF 6, diameter = 240 mm, Cytiva Europe GmbH) using a vacuum pump (Busch GmbH, R5). Note that due to the formation of nanoparticles appropriate safety precautions need to be undertaken. Appropriate safety precautions include a well-closed fume hood equipped with an efficient exhaust system with good filtration, wearing appropriate personal protective equipment (including respirators) and ensuring that all procedures are carried out exclusively by trained and experienced personnel. The powder was sieved with a 250 μm sieve to remove any filter residues. Afterwards, the catalysts were calcined at 330 °C (5 K min^{-1}) for 3 h in static air to exclude unburnt organic residues.

2.2 Characterization

ICP-OES. The metal ratio of the prepared catalyst was measured with inductively coupled plasma optical emissions spectroscopy (ICP-OES) using an Agilent 725 spectrometer with a plasma excitation of 40 MHz and 2 kW. For dissolving the samples, a solution of nitric acid and hydrochloric acid was added and the mixtures were treated with microwave irradiation at 600 W for 90 minutes an Anton Paar Multiwave 3000. The average of two measurements were used for each sample.

***Ex situ* XRD.** All catalysts were characterized through *ex situ* X-ray diffraction (XRD) analysis using a PANalytical X'Pert PRO diffractometer. The powder catalyst was measured within a 2θ range of 5° to 120°, with increments of 0.017° and a scanning speed of two steps per second. Analysis of the obtained patterns was performed using X'Pert HighScore software. The XRD measurements used Cu Kα radiation with a wavelength of 0.154 nm, and Cu Kβ

radiation was filtered out using a nickel filter. Following the subtraction of the Cu Kα radiation the resulting diffraction patterns were compared to reference diffraction patterns to identify and assign various metal phases. XRD data analysis was performed *via* Rietveld refinement using TOPAS software (v.6, Bruker AXS).[42] A LaB6 standard was used to determine the instrumental profile function, which could be described using a pseudo-Voigt Thompson–Cox–Hastings peak shape. The initial fitting of the LaB6 standard gave the *u*, *v*, *w* and *x* parameters for the peak shape description, which were fixed for the sample pattern refinement. The XRD patterns of the catalysts samples were compared with references available in the inorganic crystal structure database (ICSD, Table S4).[43–47] Crystallographic information files (CIFs) were subsequently downloaded from the ICSD and used as structure models for the fitting of the XRD pattern. The lattice parameter, scale factor and crystallite size depending on the profile broadening was refined for each structure. The errors for each refinement are given in the SI, section 1.2.

TGA. Thermogravimetry analysis (TGA) was performed to identify and quantify potential organic residues present in the unburnt precursors. The samples were placed in a crucible and heated in static synthetic air (Air Liquide) from 25 °C to 800 °C with a 5 K min^{-1} ramp using a Mettler Toledo TGA2 LF/1100/833 apparatus.

TPR. H_2 temperature programmed reduction (TPR) measurements were conducted with a Micromeritics AutoChem II 2920 analyzer to analyze the reduction behavior of the catalysts at varying temperatures. 100 mg of each catalyst (sieve fraction 100–200 μm) were dried at 330 °C (5 K min^{-1}) in 10% O_2 in Ar (50 mL min^{-1}) for 30 min and cooled to room temperature. The TPR profile was obtained by heating the samples to 350 °C at a rate of 5 K min^{-1} while being reduced in 10% H_2 in Ar at 50 mL min^{-1}. The consumption of H_2 was determined by analysis of the eluted gas using an internal, duly calibrated thermal conductivity detector (TCD) of the AutoChem analyzer.

N_2-physisorption. The specific surface area of the catalysts was assessed through N_2 physisorption at −196 °C using a BELSORP-mini II (Rubotherm), with calculations performed using the Brunauer–Emmett–Teller (BET) method in the P/P_0 range of 0.05–0.3 using Belsorp adsorptions/desorptions data analysis software. Prior to the measurement, the catalyst samples were heated at 200 °C for 1 h.

N_2O pulse chemisorption. An Altamira AMI-300 equipped with a Thermal conductivity detector was used for the combined TPR–N_2O pulse chemisorption analytic. The AMI 300 equipment is equipped with four mass flow controllers responsible for the relevant four inlets groups, allowing thus a greater flexibility regarding the gas mixtures: carrier (4 lines), treatment (4 lines), blend (2 lines) and aux(iliary) (2 lines). The chemisorption equipment was piloted *via* the proprietary steering software ("AMI 300") from the Altamira software package, using dedicated experiment programs (.exp) whereas the evaluation of the TPR and N_2O-pulsechemisorption profiles was performed using the "AMI-Analysis" part of the software package. TPR and N_2O profiles suitable for publication have been generated using the OriginPro 2022 software package (version 9.9.0.225). *Ca.* 100 mg of catalyst were placed in a U-shaped quartz reactor and first dried under argon at 120 °C (flow 30 mL min^{-1}, temperature ramp 10 K min^{-1}, holding 30 min at 200 °C) followed by cooling down to 50 °C under Ar flow (20 K min^{-1}). The temperature was raised afterwards from 50 °C to 250 °C at a rate of 1 K min^{-1} (250 °C holding for 45 min) in a gas mixture containing 5 vol% H_2/Ar (10 vol% H_2/Ar Air Liquide CRYSTAL gas mixture, flow 15 mL min^{-1} diluted with pure Ar @ 15 mL min^{-1}). The TCD was calibrated before the experiment using the same diluted 5% H_2/Ar gas mixture (flow 30 mL min^{-1}, 5 pulses, volume of the loop 518 mL). The sample being yet reduced and kept under Argon flow all the time, a rough determination of the active surface of the Cu-containing catalysts can be performed *via* N_2O pulse chemisorption according to the following reaction N_2O + 2 "Cu" → N_2 + Cu–O–Cu. The principle of the titration relies on a controlled oxidation of the surface of the sample with a mild oxidant (N_2O), sending pulses of a definite volume (again 518 mL) and quantifying the liberated N_2 *via* evaluation of the cumulated TCD surfaces measured and comparison with a definite commercial gas mixture (5 vol% N_2/helium Air Liquide CRYSTAL gas mixture). The pulse chemisorption is actually performed using a gas mixture of 5 vol% N_2O in helium (using a 10 vol% N_2O/He Air Liquide CRYSTAL gas mixture – @ 15 mL min^{-1} – diluted with pure helium @ 15 mL min^{-1}). Prior to the measurements, the system has to be thoroughly flushed with pure helium (15 min, 30 mL min^{-1} @ 50 °C). Once in a steady state, the sample is submitted to 60 pulses of N_2O, alternating pure helium- (30 mL min^{-1}) and N_2O/He pulses. The liberated N_2 pulses measured with the TCD show a typical "comb" pattern, the active surface being gradually, mildly oxidized to completion. The relatively high number of pulses combined with a low N_2O loading allows for a good precision of the measurement almost similar to the reactive frontal chromatography (RFC) method performed with continuous flow, a very low N_2O loading (1–2 vol% N_2O in He) and typically a MS detector. The TCD being with every measurement calibrated it is easy to determine *via* the Altamira analysis software the total amount of N_2 liberated and hence the oxidized surface of the catalysts according to the equation: amount absorbed/liberated in μmol = $(P \times V(\text{measured}))/(R \times T)$ with P in atm; V in μL; R = 0.08206 L atm K^{-1} mol^{-1} and T in K.

SEM-EDX. The morphology of the catalysts after calcination was examined using scanning electron microscopy (SEM). Images were recorded using a Gemini SEM 500 (Zeiss) at an acceleration voltage of 10 kV. Subsequently, for evaluation of the catalysts composition and

metal distribution, energy-dispersive X-ray (EDX) spectroscopy was carried out using a X-MaxN detector (Oxford) with an 80 mm^2 sensor active area.

HAADF-STEM-EDX. For imaging scanning transmission electron microscopy was performed using a ThermoFischer Themis 300 with a high-angle annular dark-field (HAADF) detector. Elemental distribution was examined using EDX spectroscopy with a ThermoFisher Scientific Super-X EDX detector. For sample preparation, a standard Lacey carbon grid with Cu mesh was used. To mitigate the C contamination, plasma cleaning of the samples on the TEM grid were performed using Ar–O plasma at 40% power, 30 sccm, for 40 s.

Raman spectroscopy. For analysis of the phase composition, *ex situ* and *operando* Raman spectroscopy was measured. The instrument used was an inVia Raman spectrometer (Renishaw), equipped with a frequency-doubled Nd:YAG laser (532 nm, 100 mW) and an optical microscope (Leica). For the *ex situ* measurements, the laser intensity was set to 10%, using a 2400 lines mm^{-1} grating and an acquisition time of 60 s. The spectral range was 60–1320 cm^{-1}. Per sample, 5 measurements were averaged. In case of the *operando* measurements, the setup described for the XAS measurements (see below) was used. In a borosilicate capillary, about 10 mg of the calcined sample in the sieve fraction 100–200 μm was stabilized with quartz wool. The capillary was then attached to the setup and fixed above a temperature-controlled gas blower. A fibre optics probe (Renishaw) with a distance objective was used and the 532 nm laser with a diameter of ~70 μm was focused on the sample (Fig. S15). For the *operando* measurements, 50% laser intensity was applied with an acquisition time of 60 s. A 2400 lines mm^{-1} grating was used and the spectral range was 60–1320 cm^{-1}. The experimental protocol was as follows: The catalyst was reduced in a 10% H_2 in N_2 gas flow (40 mL min^{-1}) a heating rate of 5 K min^{-1} until reaching 275 °C, holding the temperature for 1 h. Afterwards, CO_2 hydrogenation conditions were applied (230 °C, H_2/CO_2 3 : 1, 40 mL min^{-1}, 20 bar, WHSV 3 × 105 h^{-1}). After 1 h under reaction conditions, H_2 was replaced with the same volumetric amount of He, mimicking a H_2-dropout for 1 h. Subsequently, CO_2 hydrogenation conditions were again applied. Data treatment in terms of cosmic ray removal, noise filtering, truncation and baseline subtraction for the operando data and truncating, baseline subtraction and averaging in case of the *ex situ* data was done using the software WiRE4.4 (Renishaw).

***Operando* XAS.** *Operando* X-ray absorption spectroscopy (XAS) of the sample CMZ was performed at the BALDER beamline at the MAX IV Laboratory synchrotron facility, Lund University, Sweden,[48] while the operando XAS experiments for CM-Z were conducted at the ROCK Beamline at the Synchrotron SOLEIL, Saint-Aubin, France.[49,50] For each experiment, a home-build high-pressure setup (Fig. S14) was used. The desired gas flow rates were controlled through MFCs and FlowDDE software (Bronkhorst) whereas electronical as well as pneumatic valves were controlled using LabView. A continuous flow capillary reactor (borosilicate, 1.5 mm outer diameter 100 mm length, 0.05 mm wall thickness, Hilgenberg) was filled with ~7 mg SiO_2-diluted sample (sieve fraction 50–100 μm, 1 : 6 SiO_2 dilution), held between two layers of quartz glass wool and placed inside a furnace (BALDER) or above a temperature-controlled gas blower (ROCK). A thermocouple was positioned halfway into the glass wool within the capillary. Spectra were recorded at the Cu K edge (8979 eV) and the Zn K edge (9662 eV).

In case of CMZ, XAS data was collected at the BALDER beamline, MAX IV, in transmission mode with a beam size of 100 × 100 $μm^2$. The liquid N_2 cooled double crystal (Si111) monochromator (FMB Oxford, UK) was calibrated to the first inflexion point of Cu-foil (8979 eV) for the Cu K edge data collection, and to the first inflexion point of Zn-foil (9659 eV) for the Zn K-edge data collections. Both edges were recorded in alternating loops with 3 s per spectrum. The X-ray beam passed though the horizontally positioned capillary reactor and the spectra were collected by scanning 5 × 20 points along the catalyst bed. Before the experiment, after the reduction and after each feed and the H_2-dropout, spectra were recorded at room temperature for 10 minutes. The room temperature spectra were averaged for both edges to yield a single spectrum each. Data extraction, energy alignment and normalization were performed using the script provided by the beamline. Further data treatment outlined in the ESI was conducted with Fastosh software package (version 1.08)[51] and the IFEFFIT[52] software package. For the reduction procedure, the sample was heated to 275 °C in 20% H_2 in N_2 (40 mL min^{-1}, 5 K min^{-1}, 1 h hold). Subsequently, reaction conditions of a gas atmosphere consisting of H_2/CO_2 (3 : 1) in 12% N_2 (40 mL min^{-1}), 230 °C and 20 bar pressure were applied. These conditions were kept for 1 h, before replacing the H_2 with additional N_2 flow for 1 h. Afterwards, reaction conditions as described before were again applied. The experimental procedure is schematically shown in Fig. S18. During all times, the gas hourly space velocity (WHSV) was kept at 3 × 10^5 mL g_{cat}^{-1} h^{-1}. For gas analysis, a ThermoStar GSD 320 mass spectrometer by Pfeiffer vacuum was used. Between the different conditions, the reactor was allowed to cool to room temperature with a rate of 25 K min^{-1}. In case of stable conditions of the experimental procedure, no gradient throughout the catalyst bed was detected. Therefore, the scans acquired at 5 × 20 points could be merged for better visualization and comparison of the datasets. At the ROCK beamline, XAS data was collected for CM-Z in transmission mode. The double crystal (Si111) monochromator was calibrated to the first inflexion point of Cu-foil (8979 eV) and to the first inflexion point of Zn-foil (9659 eV) for the Zn K edge. The X-ray beam passed though the centre of the catalyst bed inside the horizontally positioned capillary reactor. Spectra during temperature ramps and elevated temperatures were recorded alternating between the Cu and the Zn K edge with an acquisition of each 120 s and a frequency of 2 Hz. Spectra at room

temperature before the experiment, after the reduction and after the experiment were recorded for 5 minutes for each edge region. For each acquisition loop, the spectra were averaged to yield one spectrum for each edge. The beamline software was used for energy calibration, averaging, background subtraction and normalization. The sets of spectra recorded at room temperature were averaged to one spectrum respectively for both Cu and Zn K edges. For the experiments at the ROCK beamline, an O_2 trap (Restek, Germany) was additionally integrated in parallel to the inlet line to the reactor to ensure an oxygen-free inlet gas for one stage of the experiment.[53] The capillary reactor was positioned between ionization chamber 0 and 1 and Cu and Zn foil was attached in front of ionization chamber 2, to measure beam absorption of the sample and reference foils simultaneously. The catalyst was reduced in a 20% H_2 in N_2 gas flow (40 mL min^{-1}) and a heating rate of 5 K min^{-1} until 275 °C with 1 h holding time. For CO_2 hydrogenation conditions, the temperature was decreased to 230 °C and the gas was changed to a mixture of H_2/CO_2 (3 : 1, 40 mL min^{-1}). During the reaction, a pressure of 20 bar was applied and throughout the whole experimental procedure, the WHSV was kept at 3 × 105 h^{-1}. For the subsequent hydrogen dropout experiments, system was depressurized and the inlet gas was now led through the oxygen trap. The flow of H_2 was exchanged by an additional N_2 flow. After 1 h, the oxygen trap was bypassed for another hour. Finally, the pressure during the dropout was increased to 20 bar. Between each change of settings, the reactor was allowed to cool down to room temperature at 25 K min^{-1} to record spectra at room temperature. For gas analysis, an on-line micro gas chromatograph (μ-GC) (Inficon Fusion Micro GC, PoraPLOT Q, 10 m length and 0.25 mm diameter with He as carrier gas and a molecular sieve column with 5 Å, 0.25 mm diameter, 10 m length and Ar as carrier gas) was used. The experimental procedure is schematically shown in Fig. S18.

2.3 Catalytic testing

For catalytic activity tests, the catalyst powders were pressed and fragmented using a mortar. The catalyst bed, positioned in the centre of a stainless-steel tubular reactor, was held in place by two layers of quartz wool. The catalyst bed consisted of 0.40 g catalyst (sieve fraction 300–450 μm), diluted with 1.00 g of silicon carbide SiC (Carborundum, sieve fraction 0.210 mm, VWR Chemicals). The reactor was filled with SiC (Carborundum 0.500 mm, VWR Chemicals) above and below the catalyst bed (Fig. S9). A split tube furnace (HTM Reetz GmbH) was employed to heat the reactor. The temperature was recorded using thermocouples at the bottom and top of the catalyst bed and inside the furnace. The reactor and furnace were connected to laboratory setup (Fig. S10). The setup allowed for operation at either ambient pressure or pressures up to 30 bar using a back-pressure regulator (Swagelok). The gases were dosed using mass flow controllers (Swagelok) and a flow meter (Bios DryCal Definer 220 gas flow calibrator, MesaLabs) was connected to the exhaust pipe to monitor the gas flow. For monitoring of the gas composition at the outlet, an on-line μ-GC (Agilent Technologies 490 Micro GC) was used equipped with two channels (CP-Pora PLOT U column, 10 m length with helium as carrier gas and a CP-mole sieve column of 5 Å, 10 m length and argon as carrier gas). The gas pipes after the reactor were heated to 120 °C to prevent condensation of liquid products. For activation, the catalyst was initially heated to 275 °C (heating ramp rate 5 K min^{-1}) for 1 h in a gas mixture of 10% H_2 in N_2 (both gases from Air Liquide, 99.9999%) at atmospheric pressure and a WHSV of 30 000 mL g_{cat}^{-1} h^{-1}. Following catalyst reduction, the temperature was decreased to 230 °C and the gas feed was switched to 80% H_2/CO_2 (in a 3 : 1 ratio) in N_2 (Air Liquide, 50 : 50 mix of CO_2/N_2). The reaction was conducted at 30 bar and various flow rates yielding a set of WHSV of 75 000, 37 500 and 22 500 mL g_{cat}^{-1} h^{-1}. Conditions were held for 1 h at each stage. A schematic representation of this experimental process is illustrated in Fig. S9. CO_2 conversion was calculated using N_2 as an internal standard, as described in eqn (S1) in SI. Space–time yield, methanol selectivity and carbon balance were calculated using eqn (S2)–(S4) in SI.

3. Results

3.1 Catalyst preparation and *ex situ*/*in situ* characterization

Two series of CuO/MgO/ZnO catalysts were prepared by flame-spray pyrolysis. In the first series, the Zn amount was varied between 5, 10 and 15 at% Zn respective to the total metal content (Cu, Mg, Zn) and a brief comparison of the three catalysts is provided in Fig. 1. These catalysts were prepared using the double-flame FSP configuration, with Zn in the second flame. Across 5/10/15% Zn containing samples, ICP confirmed the targeted metal ratios (Fig. 1a). H_2-TPR evolves from a single broad event at 5% Zn (176 °C) to two-step profiles at higher Zn (Fig. 1a). The two reduction events occur at 141 °C and 204 °C for CM-Z10 and 152 °C and 195 °C for CM-Z15. The lower temperature signal for the 10 and 15% Zn loading could result from finely dispersed, highly accessible Cu species which reduce more easily while the

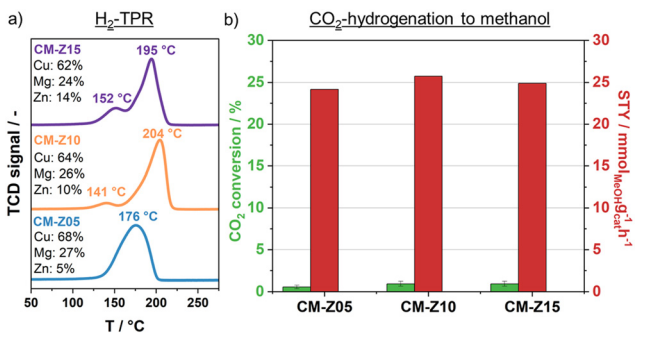

Fig. 1 a) H_2-TPR profiles (5 K min^{-1}, 10% H_2/Ar, 50 mL min^{-1}) and b) CO_2 conversion and STY for methanol during CO_2-hydrogenation (230 °C, H_2/CO_2 = 3 : 1, 30 bar, WHSV = 75 000 mL g_{cat}^{-1} h^{-1}, 1 h hold).

second reduction peak arises from bulk Cu reduction.[54,55] An alternative explanation is the stepwise reduction of $Cu^{2+} \rightarrow Cu^{+} \rightarrow Cu^{0}$, in which the Cu^{+} could be stabilized by a higher Zn loading.[56–58] Raman spectroscopy exhibited bands referring to CuO and ZnO.

Under CO_2-hydrogenation conditions at 230 °C and 30 bar, CO_2 conversion levels were the same for CM-Z10 and CM-Z15 (1.0%), while the 5% Zn loading lead to a lower conversion (0.5%). Considering the methanol yield, 10% Zn delivers the highest space–time yield (STY, 13.3 mmol MeOH g_{Cu}^{-1} h^{-1}) of the three catalysts (12.3 and 11.6 mmol MeOH g_{Cu}^{-1} h^{-1} for CM-Z05 and CM-Z15, respectively, Fig. 1b). On this basis, we fixed Zn at 10% and used FSP flame configuration to tune Cu–Mg–Zn proximity. Single flame (CMZ) co-sprays all precursors, whereas double flame partitions them (CM-Z, CZ-M, C-MZ) (Fig. S1), enabling controlled co-nucleation *vs.* late mixing. We note here that the catalyst previously designated as CM-Z10 in the compositional screening will from this point forward be denoted simply as CM-Z. This shorthand emphasizes that within this second set of catalysts, the elemental composition remains constant at 10 at% Zn, while only the flame spray configuration is varied. Aim of this design strategy of a series of model catalysts was to elucidate the impact of Cu–Mg, Cu–Zn and Mg–Zn interactions, targeting systematic changes in reducibility and operando redox stability that reinforce MeOH productivity. During single flame synthesis, the solution contained all metal precursors, while for the synthesis with two nozzles and flames, the metal precursors where separately dissolved in two solutions, which resulted in a set of three ways of combining the precursor solutions (Table 1): Cu + Mg *vs.* Zn, Cu + Zn *vs.* Mg and Cu *vs.* Mg + Zn. The catalysts eventually obtained were named depending on the flame configuration (CMZ, CM-Z, CZ-M and C-MZ). The Cu, Zn and Mg precursors exhibit different decomposition temperatures, which mark their final transition into the corresponding metal oxides. An overview on the different temperatures found in literature is presented in Table S1. From reports, copper acetate monohydrate and zinc acetate dihydrate exhibit a similar decomposition temperature between 275 °C and 310 °C, depending on the conditions.[59–62] Magnesium acetate tetrahydrate exhibits the highest reported decomposition temperature (345 °C) for the full oxidation towards MgO.[63] The temperatures in a methane/oxygen flame used during synthesis is expected to reach temperatures exceeding 1500 °C, theoretically allowing all components to transform into the metal oxide.[64] Relevant for the nucleation process and the mixing of components is their "volatility" or stability, which can be qualitatively assessed through information on melting point, boiling point and vapor pressure of the metal oxides. CuO exhibits the lowest stability among the produced metal oxides and tends to decompose at high temperatures (>1000 °C).[65,66] Based on several reports on vaporization and vapor pressure, ZnO is prone to sublimation at high temperature above 1300 °C.[67,68] Due to its higher thermal stability and high vaporization temperature (1800 °C),[69] MgO is assigned with the lowest volatility in the set of metal oxides. Hence, it is assumed hat MgO solidifies first, followed by ZnO and CuO, setting MgO as main support structure. As reported by Samerjai *et al.*,[70] the formation of $Mg_xZn_{1-x}O$ nanocomposites was observed for single flame synthesis. For combinations of Cu with Zn or Mg, no such nanocomposites are reported in literature. As the nozzles in the two-flame method were tilted by 30° toward each other, the flames and the forming particles met relatively late. This results in a shorter interaction time for the pyrolyzed precursors and a reduced mixing prior to quenching. Calcination of the sample resulted in an overall weight loss of *ca.* 0.5% (Table S2) as unburned residues were eventually combusted. Prior to activity test, the calcined catalysts were characterized using various analytical methods. According to ICP-OES, the aimed atomic metal ratios were achieved (Table S3) with 65 ± 1% Cu, 25 ± 1% Mg and 10 ± 1% Zn relative to each other.

XRD patterns of the calcined catalysts reveal reflexes assigned to CuO, MgO and ZnO (Fig. 2). In contrast to other studies,[71,72] no clear shift in the reflexes is observed compared to literature reports for MgO.[46] Due to the missing of a Mg free sample, shift originating from an incorporation of Cu ions into the lattice cannot be excluded. Qualitatively, all calcined samples contained the same metal oxides as the diffraction could be assigned to crystalline CuO, MgO and

Table 1 Catalysts prepared by FSP in single flame (A) or double flame (A + B) to tune the direct interaction between Cu–Mg, Cu–Zn and Mg–Zn

Catalyst	Cu/Mg/Zn atomic ratio	Flame A	Flame B
CMZ	65/25/10	Cu, Mg, Zn	—
CM-Z	65/25/10	Cu, Mg	Zn
CZ-M	65/25/10	Cu, Zn	Mg
C-MZ	65/25/10	Cu	Mg, Zn

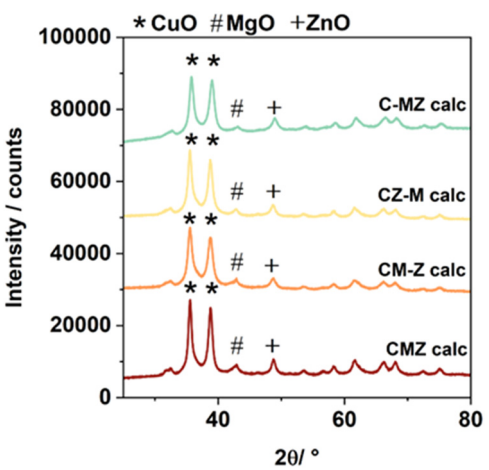

Fig. 2 XRD patterns of the calcined CuO-ZnO-MgO catalysts (for the abbreviations please refer to Table 1).

Table 2 Crystalline phases and their fractions of the calcined catalysts as determined by Rietveld refinement. Details on the refinement results are given in SI section 1.2

	Phase composition and crystallite sizes *via* Rietveld refinement/wt%					
Calcined	MgO/wt%	MgO cryst. size/nm	ZnO/wt%	ZnO cryst. size/nm	CuO/wt%	CuO cryst. size/nm
CMZ	28.1	6	5.4	5	66.5	13
CM-Z	29.1	5	5.6	5	65.2	10
CZ-M	17.3	8	7.4	5	75.3	11
C-MZ	19.9	6	5.2	5	77.6	11

ZnO for all catalysts (Table S4). For a qualitative and quantitative analysis of the crystalline phases, Rietveld refinement of the XRD pattern was employed (Fig. S3 and S4, Tables S5–S8). Crystalline ZnO/MgO mixed structures could be excluded through comparison with literature.[73–75] Additionally, the crystallite size was determined for CuO (Table 2).

When comparing the catalysts, the determined fraction of crystalline CuO is higher for the cases in which Mg and Cu were sprayed in separate flames (CZ-M and C-MZ). Thus, the direct contact and interface with MgO during synthesis impacts the crystallinity of Cu. The crystallite size of CuO ranges from 10 nm for CM-Z to 13 nm for CMZ prepared by single flame pyrolysis, while the ZnO crystallite size remained unaffected by the flame configuration and accounted for 5 nm for all samples. The MgO crystallite size on the contrary varied between the flame configurations, showing the largest crystallites (8 nm) for CZ-M in which only Mg is sprayed separately. CMZ and C-MZ exhibit the same MgO crystallite size of 6 nm according to the Rietveld refinement and for both samples, Zn and Mg were dosed in the same flame. This demonstrates that the presence of Zn in the same flame impacts the MgO crystallite size. Moreover, the results in Table 2 show an inverse relationship between the CuO and MgO phase fractions determined *via* the refinement: larger MgO phase fractions correlate with lower CuO fractions and *vice versa*. This furthermore amplifies the close interaction and interdependency of the components.

With Raman spectroscopy, bands referring to CuO (275, 314, 605 cm^{-1}),[23,76–78] and ZnO nanocrystallites (559 cm^{-1})[79–84] were clearly identified for all calcined catalysts (Table S9). This will be discussed later together with the Raman spectra recorded of the spent catalyst.

The spatial distribution of the elements was investigated using STEM (Fig. S5–S7) and HAADF TEM (S8) with corresponding EDX mappings. A homogeneous distribution of the elements Cu, Mg, Zn and O could be confirmed for all catalysts. From the HAADF-STEM-EDX images, all three metal components seem to be superimposed for all probed catalysts and no clear microstructural differences can be observed within the selected but still representative areas. Apart from imaging techniques, other characterization methods revealed different properties or behaviors among the set of catalyst.

The temperature-programmed reduction (TPR) with H_2 revealed significant differences between the catalysts (Fig. 3a). The catalyst with the lowest Zn amount (5%, CM-Z05) exhibits one broad signal, while all other catalysts show two distinct reduction events. This might indicate that above a certain Zn fraction, a Cu–Zn–Mg composite structure could be formed, in which the catalyst components are strongly interconnected. The development of such a composite structure may give rise to the two reduction peaks observed in the H_2-TPR profiles. The lower temperature signal could either result from finely dispersed, highly accessible Cu species which reduce more easily[54,55] or from a stepwise reduction of $Cu^{2+} \rightarrow Cu^{+} \rightarrow Cu^{0}$.[56,57] Among the samples, C-MZ reduces at the lowest temperature (main peak at 184

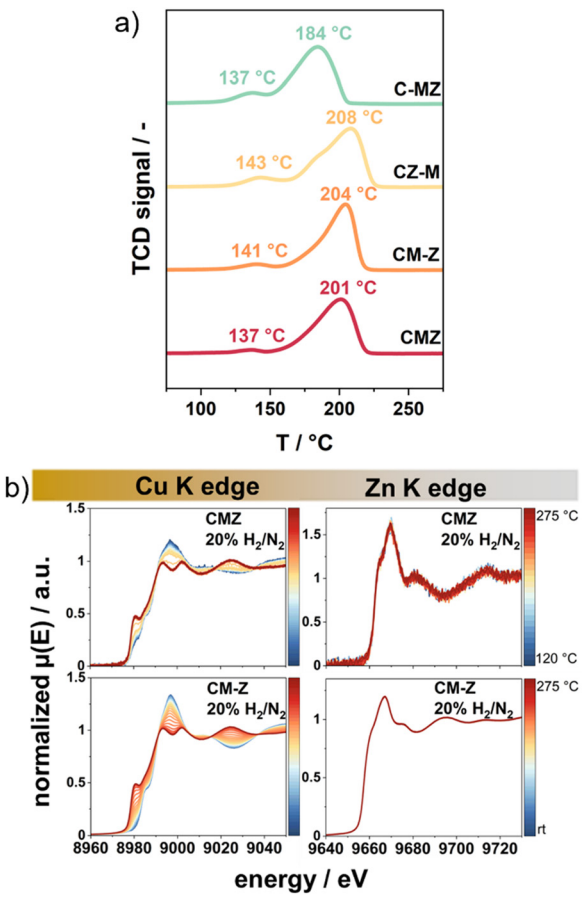

Fig. 3 a) H_2-TPR profiles of the catalysts. b) XANES spectra at the Cu K edge and Zn K edge during TPR (20% H_2 in N_2, 275 °C, 5 K min^{-1}) for CMZ at the Balder Beamline at MAX IV and CM-Z at the ROCK Beamline at Soleil Synchrotron.

°C), similar to CM-Z05 (Fig. 1), followed by single-flame CMZ (201 °C), CM-Z (204 °C) and CZ-M (208 °C). The reduction of Cu in CMZ and CM-Z is clearly visible in the XANES spectra during *in situ* TPR (20% H_2/N_2, 275 °C, 5 K min^{-1}, Fig. 3b), evident by the gradual change in energy of the absorption edge and shape of the spectra over the course of the reduction step. In the beginning, Cu is present in the fully oxidized state (CuO), while upon TPR, a pre-edge shoulder and the double-peak typical for metallic Cu evolve (Fig. 3b). In contrast, changes in the Zn K-edge spectra are hardly visible. Quantification of reduced and oxidized Cu and Zn states by linear combination analysis (LCA) is discussed later in the *operando* XAS section. The broadening of the reduction peak and its appearance at lower temperatures for C-MZ (Fig. 3a) and CM-Z05 (Fig. 1a) suggests a wider distribution of Cu environments, including particle size. In contrast, a shift towards higher reduction temperature for CMZ, CM-Z and CZ-M might indicate a stronger developed composite, in which Cu is stronger interfering with Zn and Mg, making it harder to reduce.[23] A partial reduction of Zn within a CuZn alloy could not be determined in TPR due to possible overlapping with H_2 consumption for the large Cu fraction.

The specific surface area was determined by N_2-physisorption, revealing variation among the catalyst series between 39 and 53 $m^2\ g^{-1}$as provided in Table 3 (and Table S10 for the CM-Z catalyst with varying Zn%). Comparing single-flame and double-flame configuration shows a smaller specific surface area for the single-flame catalyst (39.4 $m^2\ g^{-1}$), which again indicates larger particles. This observation is in line with XRD refinement, for which larger crystallite sizes were found for CMZ. Generally, the surface areas of the obtained catalysts are lower compared to other flame-sprayed materials, especially compared to Cu catalysts with a much higher Zn fraction.[37] In contrast, the surface area is higher compared to other Cu/Mg or Cu/Zn/Mg catalysts found in literature.[23,24] According to these reports, especially the incorporation of Mg was responsible for higher surface area compared to unpromoted Cu Cu or Cu/Zn catalysts.[23,24] Furthermore, N_2O-Chemisorption was applied to determine the metallic surface area (Cu^0 + Zn^0) relevant for the reaction mechanism (Table 3). These surface areas are larger than values provided for Cu/Al_2O_3 and Cu/MgO catalysts in literature,[21] keeping in mind that the specificity of the chemisorption equipment and of the programs used for the different measurements makes a direct comparison for the metallic surfaces challenging. In line with the N_2-physisiorption results, the single-flame synthesized catalyst CMZ revealed a lower metallic surface area (13 $m^2\ g^{-1}$), which is significantly smaller than those measured for CM-Z (21 $m^2\ g^{-1}$), CZ-M (23 $m^2\ g^{-1}$) and C-ZM (19 $m^2\ g^{-1}$). This furthermore amplifies the assumption that single-flame sprayed particles are larger compared to the double-flame method and hence provide fewer Cu–ZnO or Cu–MgO interfaces. However, differences in particle sizes could not be confirmed with imaging techniques such as SEM and TEM.

Table 3 N_2-physisorption (BET, specific surface area) and N_2O-chemisorption (metallic surface area, Cu^0+Zn^0) of catalyst prepared by FSP in the modes single flame (CMZ) and double flame

Catalyst	BET specific surface area[a]/$m^2\ g^{-1}$	Metal surface area[b]/$m^2\ g^{-1}$
CMZ	39 ± 1	13 ± 1
CM-Z	53 ± 1	21 ± 1
CZ-M	41 ± 1	23 ± 1
C-MZ	49 ± 1	19 ± 1

[a] N_2-physisorption. [b] N_2O-titration.

3.2 Catalytic activity and characterization of spent catalysts

The CO_2 conversion (eqn (S1)) and space–time yield (STY, eqn (S2)) of the various catalyst at the weight-hourly space velocities of 22 000, 37 500 and 75 000 mL $g_{cat}^{-1}\ h^{-1}$ at 230 °C, 30 bar, H_2/CO_2 = 3 : 1 in N_2, are depicted in Fig. 4. The error bars originate from deviations within one hour of measurement per space velocity. Schemes of the reactor and setup and the experimental schedule are provided in Fig. S9–S11. Table S11 contains the masses of catalyst and diluent used for reaction. High methanol selectivity was achieved for all catalysts (Table S12), reaching from *ca.* 80% for CZ-M at 37 500 mL $g_{cat}^{-1}\ h^{-1}$ to 100% for all catalysts at the highest space velocity while at the same time reaching a closed carbon balance (Table S13). In general, the conversion of CO_2 decreases with increasing space velocity due to lower residence time, which can be observed in Fig. 4a. The CO_2 conversion is similar for all catalysts especially at 22 000 mL $g_{cat}^{-1}\ h^{-1}$, ranging from 1.75 to 1.9%. In particular CMZ and CM-Z reveal the same CO_2 conversion (1.77%) for the lowest tested WHSV and similar conversions for the higher WHSV. Apart from CZ-M, the STY of methanol for catalysts rises with increasing WHSV, as a higher space velocity suppresses secondary reactions (reverse water–gas shift, eqn (3)).[85] Due to the similarity of the selectivity values and to also account for the varying CO_2 conversion, the space–time yield (STY) was calculated, capturing the methanol production per time unit normalized to the mass of catalyst. Among the catalysts, the single-flame catalyst shows the highest STY (~29 $mmol_{MeOH}\ g_{cat}^{-1}\ h^{-1}$) together with double flame made C-MZ (~29 $mmol_{MeOH}\ g_{cat}^{-1}\ h^{-1}$) and CM-Z (~26 $mmol_{MeOH}\ g_{Cu}^{-1}\ h^{-1}$). For the WHSV of 22 000 and 37 500 mL $g_{cat}^{-1}\ h^{-1}$, the STY values for CMZ and CM-Z are very similar. The obtained values for the methanol production (STY) for all catalysts are in comparable or higher range compared to similar catalyst reported in literature, from which most are prepared *via* coprecipitation. A conclusive list of reference catalysts, the respective composition and STY are provided in Table S14. The literature reported STY ranges from 8 to 17 $mmol_{MeOH}\ g_{cat}^{-1}\ h^{-1}$, which is in the same range or lower than the STY achieved in our study for the lower and intermediate space velocity.[23,24,86–88] For the highest space velocity, our CMZ catalysts reach significantly higher values, reaching up to 29 $mmol_{MeOH}\ g_{cat}^{-1}\ h^{-1}$. Interesting for CZ-M is the high methanol yield of 15 $mmol_{MeOH}\ g_{Cat}^{-1}\ h^{-1}$ at the lowest WHSV (22.500 mL $g_{cat}^{-1}\ h^{-1}$). In the course of the experiment

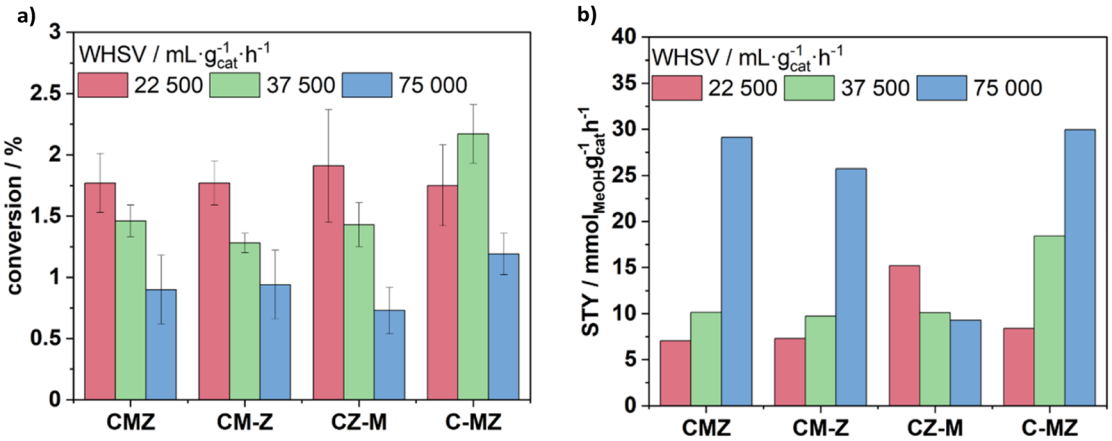

Fig. 4 a) CO_2-conversion and b) space–time yield (STY) of methanol of the catalysts at 3 different weight hour space velocities (WHSV) during CO_2-hydrogenation conditions (230 °C, 80% H_2/CO_2 (3 : 1) in N_2, 30 bar).

the WHSV was increased, but contrary to the other catalysts, the methanol yield decreased for CZ-M, implicating loss of selectivity towards methanol. As typically, STY of methanol increases with increasing WHSV, it is assumed that this deactivation occurs due to the duration of the activity measurement. This pronounced loss of methanol selectivity over time leads to the conclusion that MgO indeed affects the catalysts stability and long-term selectivity of CuZn catalysts and that a pronounced integration of Mg during the spraying is important to the catalyst stability. When sprayed separately, Mg cannot fulfil its promoting role, likely due to a more pronounced separation from the active components and fewer shared interfaces. Interestingly, when Mg is sprayed with Zn in the same flame and Cu in another (C-ZM), no deactivation effect could be observed within the experiments. This highlights the importance of bringing MgO in direct contact with one of the active components (Cu or Zn) in a joined flame. The spent catalysts were investigated with XRD and Raman spectroscopy. The Rietveld refinement of the XRD pattern revealed the crystalline phases and their quantity of the catalysts provided in Table 4. Based on the analysis, the crystalline phases consisted of MgO, ZnO, CuO, Cu_2O and metallic copper. It should be noted, that the spent samples were exposed to air after taken from the reactor. It is therefore not surprising to find Cu partially oxidized with Cu_2O (Cu^+) being more common than CuO (Cu^{2+}) in all catalyst except CM-Z. Furthermore, the crystallite size of Cu was determined based on Rietveld method. The single-flame catalyst exhibits the largest crystallite size for reduced Cu (15 nm), while the largest CuO crystallite size is found for C-MZ (19 nm). Overall, the Cu_2O crystallite size is similar for all catalysts. In case of ZnO, the crystallite size differs for the catalyst in which Zn was sprayed separately (CM-Z, 10 nm), while it is the same for the rest of the catalysts (7 nm). The crystallite size of MgO varied between 9 for CMZ and CM-Z and 13 nm for C-MZ. Generally, the crystallite sizes of the different components in the spent samples vary mostly independent of the flame configuration. Similar to the calcined samples, bands referring to CuO and ZnO could be identified in the *ex situ* Raman spectra of the spent catalyst (Fig. 5). All Raman spectra show spectral features assigned to bending vibration in CuO at 275 cm^{-1} (A_g),[76,77] two bands at 314 and 605 cm^{-1} caused by symmetrical stretching of oxygen in CuO (B_g)[76,77] and a band at 1112 cm^{-1} that is assigned to disorder-induced double phonon band of CuO.[23,78] The later band was shown to be enhanced by the incorporation of MgO in Cu catalysts, demonstrating a close interaction between CuO and MgO.[23] Interestingly, the band at 605 cm^{-1} is slightly more pronounced in the spent samples compared to the fresh calcined samples. The oxidic phases of Cu originate from the exposure to air after the reaction. Moreover, Raman spectra of the calcined and spent samples exhibit a band at 559 cm^{-1}, assigned to nanocrystalline ZnO.[79–84]

Table 4 Crystalline phases and phase fractions of the spent catalysts as determined by Rietveld refinement. Details on the refinement results are given in SI section 1.2

	Phase composition and crystallite size *via* Rietveld refinement/wt%									
Spent	MgO/wt%	Cryst. size/nm	ZnO/wt%	Cryst. size/nm	CuO/wt%	Cryst. size/nm	Cu_2O/wt%	Cryst. size/nm	Cu/wt%	Cryst. size/nm
CMZ	20.6	9	3.8	7	5.4	7	17.0	5	53.3	15
CM-Z	17.8	9	1.4	10	20.3	5	13.9	4	46.6	12
CZ-M	20.2	10	2.9	7	9.2	11	10.1	5	57.6	14
C-MZ	15.6	13	3.8	7	1.5	19	11.7	4	67.5	13

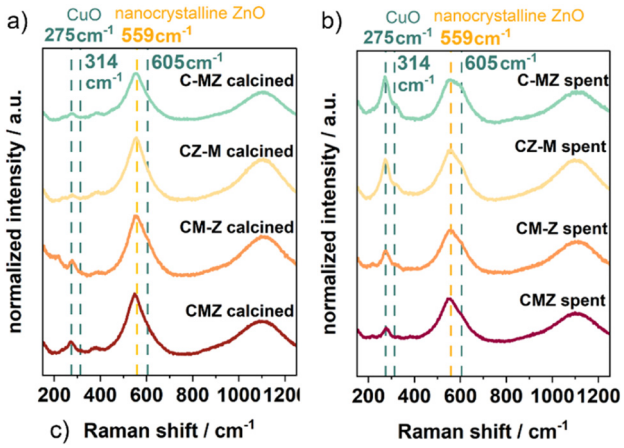

c)

band position / cm^{-1}	associated band
275	CuO (A_g)[69, 70]
314	CuO (B_g)[69, 70]
605	CuO (B_g)[69, 70]
1112	CuO[23, 71]
559	nanosized ZnO (E_1)[72-77]

Fig. 5 Raman spectra of the catalysts a) after calcination (calc) and b) spent with the associated bands indicated as dotted lines and provided as table (c).

In summary and despite the different surface areas, CMZ (single-nozzle FSP) and CM-Z (double-nozzle FSP) perform relatively similarly, especially at the lower space-velocities, indicating that specific or active surface area is not the only performance indicator on the catalyst activity, but rather sets the interaction between the catalyst components CuO, ZnO and MgO into focus. This assumption needs further characterization of both Cu and Zn species during operating conditions, which was done using XAS as described in the following paragraph.

3.3 *Operando* spectroscopy during hydrogen-dropout experiments

Operando Raman spectroscopy was performed on the whole set of flame sprayed catalysts. As collected, Raman spectroscopy mainly tracks gas-phase bands (H_2, CO_2) and signals from the capillary overlap oxide bands, so the dataset mainly reflects gas-phase monitoring under pressure, and can thus not be used to discuss the catalysts. A scheme of the gas-dosing setup, the experimental procedure and the *operando* spectra are provided in Fig. S12–16 in the SI.

Operando XAS was used to investigate the impact of the spraying mode and on the resulting catalyst oxidation state during TPR, CO_2 hydrogenation and H_2-dropout for two catalysts, CMZ (single flame) and CM-Z (double flame). Details on the setup at the beamline, data analysis, experimental schedule and gas phase analysis is provided in the SI (Fig. S17–S22). According to linear combination fitting with reference spectra of Cu foil, Cu_2O and CuO, the temperature-programmed reduction step shown in Fig. 3b ultimately resulted in the complete reduction of Cu in CM-Z, while *ca.* 13% of Cu in CMZ stayed in the Cu^+ state (Table 5a). Interestingly, the two catalysts showed similar reduction temperatures in lab H_2-TPR, with CMZ exhibiting broader signals. This broadening and the lower degree of reduction in the XAS experiment for the single flame CMZ could results from larger particles as already indicated by larger CuO crystallite size found according to XRD analysis. Upon reaction conditions, no changes for the Cu K edge XANES spectra occur for double-flame CM-Z as Cu remains in the reduced state (Fig. 6 and S23). For the single flame sprayed CMZ, the fraction of Cu^0 increased to 98% upon applying reaction conditions, which could be explained by the excess of the reducing agent H_2 in the reaction gas mixture as the conversion is low (Fig. S20 and S22). As it can be already qualitatively observed in Fig. 6 (after dropout), the H_2-dropouts lead to partial Cu re-oxidation towards Cu^+ (26%) for the single-flame sprayed CMZ, whereas Cu in double-flame sprayed CM-Z remains completely reduced (Table 5a, Fig. S24 and S25). The partial re-oxidation of Cu in CMZ induces changes in the XANES as in the pre-edge feature at 8982 eV and the increased intensity of the first main peak differs from Cu foil reference. At this point, it is important to point out the different H_2-dropout programs applied for the two catalysts. While for CMZ the exchange of H_2 with N_2 was rapid and immediately at 20 bar CO_2/N_2 mixture, CM-Z was first exposed to a H_2-dropout at ambient pressure for 30 minutes while an oxygen-trap was installed before the line. The oxygen trap was installed to exclude oxidation by possible traces of oxygen in CO_2 supply. As no changes in the XANES were observed (Fig. 6), the oxygen-trap

Table 5 Linear-combination fitting results for CMZ and CM-Z spectra at (a) Cu and (b) Zn K edge at different states of the reaction protocol

		a)				b)		
State	Catalyst	Cu^{2+}	Cu^+	Cu^0	*R*-value of fit (Cu)	Zn^{2+}	Zn^0	*R*-value of fit (Zn)
Initial	CMZ	1.00	0	0	3.0×10^{-3}	1.00	0	6×10^{-3}
	CM-Z	1.00	0	0	9.6×10^{-2}	1.00	0	8×10^{-3}
After TPR	CMZ	0.01	0.13	0.87	1.6×10^{-2}	0.99	0.01	5×10^{-3}
	CM-Z	0.01	0.01	0.98	3.0×10^{-3}	0.89	0.11	4×10^{-3}
After feed	CMZ	0	0.07	0.93	3.0×10^{-3}	1.00	0	3×10^{-3}
	CM-Z	0.01	0.01	0.98	4×10^{-5}	0.93	0.07	6×10^{-3}
After dropout	CMZ	0.05	0.26	0.69	2×10^{-5}	1.00	0	6×10^{-3}
	CM-Z	0.01	0	0.99	3×10^{-5}	0.95	0.05	6×10^{-3}

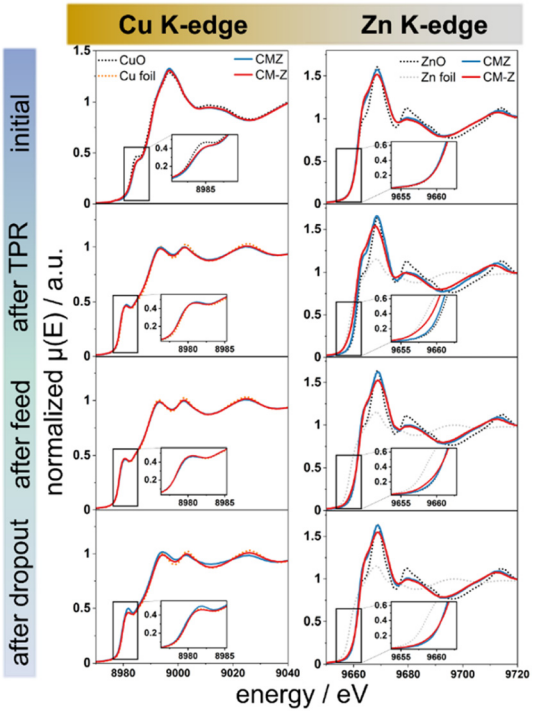

Fig. 6 Comparison of the XANES region of CMZ and CM-Z at Cu K edge and Zn K edge in initial state, after TPR at 275 °C in 10% H_2/N_2, WHSV of 3×10^5 h^{-1} for 1 h, after feed of H_2/CO_2 (3 : 1) in 10% N_2, WHSV of 3×10^5 h^{-1} at 20 bar for 1 h at 230 °C and after H_2-dropout, in which temperature, pressure and WHSV was kept but the flow of H_2 flow was exchanged by N_2. All spectra were recorded at room temperature. References are Cu foil and CuO for the Cu K edge and Zn foil and ZnO for Zn K edge spectra.

was bypassed for 30 minutes. Also, without oxygen-trap attached to the inlet gas supply, the spectra did not show any differences. Finally, the pressure of the CO_2/N_2 atmosphere in the setup and reactor was increased to 20 bar and according to XANES overlapping with the Cu foil reference, still no re-oxidation of the sample took place (Fig. S26). A passivating effect of slowly increasing the CO_2 pressure to the system cannot not be excluded, although it has never been reported in literature.

LCA fitting was also applied for the spectra recorded at the Zn K edge and the results are provided in Table 5b. In the beginning, the Zn K-edge spectra of the catalysts and the ZnO references exhibit the same Cu K edge energy, indicating the fully oxidized state of Zn in both CMZ and CM-Z. Differences become again visible through the degree of reduction after TPR as the double-flame sprayed catalyst exhibits a 11% reduction of Zn to metallic state while Zn in the single-flame sprayed catalyst stays nearly unreduced (1% Zn^0). This calculation is in line with qualitative observations of the Zn XANES spectra. As provided in Fig. 6, the position of the Zn K edge for CM-Z (9660.9 eV) shifts towards lower energies compared to the ZnO reference (9661.4 eV) and CMZ (9661.4 eV), getting closer to the Zn K edge energy of Zn foil (9658.6 eV). During reaction gas feed and H_2-dropout, Zn stays in completely oxidized state in case of the single flame sprayed catalyst CMZ, evident by the constant Zn K edge energy and spectral features. The fraction of reduced Zn in the double-flame sprayed CM-Z decreases upon feed conditions and H_2-dropout to 7 and 5%, respectively, according to LCA (Table 5b). In summary, the double-flame catalyst CM-Z shows generally a higher degree of reduction for both Cu and Zn upon TPR procedure and stability of the reduced phases during feed and H_2-dropout. By contrast, the single-flame sprayed CMZ exhibits significant re-oxidation towards Cu^+ during the dropout and generally no bulk reduction of Zn according to LCA.

4. Discussion

FSP was successfully employed for the preparation of Cu–Mg–Zn catalysts with the targeted metal ratios using different flame configurations and thus allows to further develop this method from earlier reports on FSP-derived methanol catalysts.[32–36] Despite different decomposition temperatures of the precursors, all organic salts were burned to the respective metal oxides. Co-spraying components modulates CuO/MgO crystallite sizes (Rietveld). According to Rietveld refinement of the diffraction patterns of the calcined samples, both MgO and CuO crystallite sizes were sensitive to flame configuration, indicating that the synthetic route directly influences metal–metal oxide interactions. The inverse relationship found between CuO and MgO phase fractions further supports a strong Cu–Mg interdependence in the FSP-derived materials, showing how flame co-spraying controls component proximity and shared interfaces.

The reduction behavior, assessed by H_2-TPR, strongly depended on the degree of metal–support interaction between Cu, Zn, and Mg oxide. The catalysts with lowest Zn content (5%) displayed a single Cu reduction feature, while higher Zn loadings or stronger Cu–Zn proximity produced two-step reduction profiles. Such an influence of the interaction between Cu and Zn has been reported earlier[89,90] but demonstrates the ease of tuning the metal–support interaction using the different modes of the FSP-synthesis. These profiles suggest the coexistence of weaker bound, easily reducible Cu species alongside Cu species intimately associated with other oxides, which reduce at higher temperatures. When CuO was synthesized in a separate flame from MgO and ZnO, its lower reduction temperature indicated lower interaction with the promoters alongside fewer Cu-metal oxide interfaces. Co-spraying Cu with Mg yielded the highest surface area. Interestingly, such a stabilization is also found in other preparation methods where calcination is used as last preparation step.[23,24] These findings demonstrate how component proximity governs catalysts' reducibility.

Fig. 7 summarizes the key findings of this study, demonstrating how the spray parameter governs the mixing of the catalyst components, therefore affecting its surface area, activity and stability. The extent of mixing within the components is indicated by hatched areas. Fig. 7

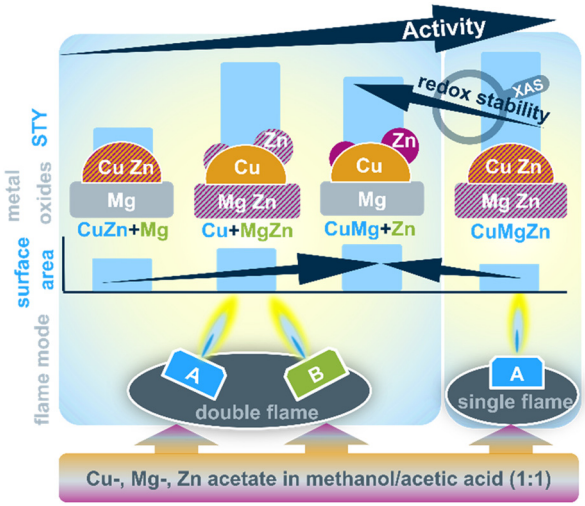

Fig. 7 Schematic presentation of the impact of flame configuration on interaction between components, surface area, yield (STY) of methanol and Cu redox stability.

emphasizes that when combining all three precursors in one flame (Fig. 7, right side), the surface area (indicated by the lower blue bars) was significantly reduced, possibly caused by the enhanced interaction of the Cu, Zn, Mg components hindering a more dispersed structure. Despite the lowest surface area, the single flame CMZ shows similar CO_2 conversion and STY (upper blue bars in Fig. 7) as the other catalysts, especially when comparing with CM-Z, where Zn was sprayed separately. Possibly, the enhanced proximity caused by the spraying in the same flame caused enhanced Cu–MgO–ZnO interfaces and metal–support interaction beneficial for catalytic activity. For the catalyst in which the Cu-compound was sprayed separately, a deactivation during the catalytic testing was observed, hinting towards a lower interaction with the support of ZnO and MgO. Generally, the space time yield (4–16 $mmol_{MeOH}\ g_{Cu}^{-1}\ h^{-1}$) is comparable or even higher than literature reports (section 3.2).[23,24] Raman spectroscopy revealed a pronounced structural evolution during operation, *e.g.*, more pronounced CuO bands after catalysis. *Operando* XAS further uncovered a different redox dynamic: in CM-Z, where ZnO was introduced separately, Zn was partially reduced during reaction, whereas in CMZ strong metal mixing appeared to hinder Zn reduction. Under H_2 dropout conditions, Zn in CM-Z readily reoxidized while Cu remained stable, suggesting that reduced Zn may act as a sacrificial species protecting Cu from oxidation, similarly as reported for Fe–Ni-based catalysts where Fe take the sacrificial role.[41] In CMZ without reduced Zn, by contrast, Cu exhibited slight reoxidation during the H_2-dropout and therefore a lower redox stability. The STY trends emphasized in Fig. 7 and deactivation behavior (CZ-M) point to the importance of bringing Mg into direct contact with at least one active component during FSP, prescribing clear synthesis guidelines for future FSP Cu–Zn–Mg MeOH catalysts.

Overall, interactions between Cu, Mg and Zn can be tuned using FSP as preparation method and the results highlight the importance of the right choice of co-feed precursors to promote the metal–metal oxide interaction through shared interfaces, activity and stability of the catalyst, as highlighted by the hatched areas and arrows in Fig. 7. With the joined combustion of all three components in one flame, a catalyst with small surface area but pronounced metal–metal oxide interaction can be obtained, leading to a high activity respective to the catalyst surface. This preparation method of simultaneous combustion of all precursors can be seen as a one-step equivalent of the more common two-step co-precipitation of Cu, Mg and Zn salts plus subsequent calcination or as an alternative to a lengthy hydrothermal synthesis.[23,91] Analogue to impregnation of a co-precipitated structure,[26] FSP can furthermore be used as one-step preparation method, in which the particle formation of the components can be separated from each other, allowing a tailored catalyst design. As an outcome of the separation of particle formation, when ZnO is sprayed "on top" of Cu–MgO, its reducibility is enhanced according to XAS experiments. This increases the stability of the Cu^0 phase during H_2-dropout conditions. With the activity during CO_2-hydrogenation being close to the performance of CMZ, this double flame configuration (CuMg + Zn) is preferred.

The collective observations underline the significant role of MgO in determining catalyst structure and function, which was declared in literature.[91] MgO is indeed no inert support, but strongly influences elemental dispersion, reducibility and catalytic behavior. This is parallel of the promoting effects known for Al_2O_3 in conventional Cu–Zn–Al systems. Like Al_2O_3, MgO can participate in mixed-phase formation with Zn as reported by Samerjai *et al.*[70] and appears to benefit from close contact with Cu, enhancing methanol synthesis activity. Just as mixed oxide phases like $CuAl_2O_3$ are reported,[92] it is assumed that Cu is imbedded in a composite-like structure with MgO and possibly even MgO and ZnO. These findings highlight MgO as an active structural and electronic promoter rather than a passive support, offering design opportunities for next-generation Cu-based CO_2 hydrogenation catalysts.

5. Conclusions

This study demonstrates that flame spray pyrolysis is a well-suited method for preparing multicomponent systems and enables precise control over Cu–Zn–Mg interactions with tunable CuO (10–13 nm) and MgO (6–8 nm) crystallites depending on flame configuration. Co-spraying strongly dictates catalyst structure and phase proximity, reducibility and performance in CO_2 hydrogenation to methanol. By varying flame configuration and precursor distribution, we were able to tune metal mixing, crystallite size, and surface area, revealing that co-spraying all components in a single flame promotes the strongest metal–support interactions, as indicated by the hatched area in Fig. 7. In terms of

reducibility, higher Zn shares and specific co-spray modes yield two-step TPR profiles, while C-MZ reduces at the lowest temperature. Although the CMZ configuration produced the lowest surface area, it delivered a catalytic performance comparable to the catalysts with higher surface areas, indicating that optimized Cu–MgO interaction can compensate for lower number of Cu^0 sites. *Operando* characterization further showed that these interactions influence redox behavior, with partially reduced Zn stabilizing Cu^0 in systems where the metals were less intimately mixed, with CM-Z maintaining Cu^0 under H_2-dropout, while CMZ partially re-oxidized to Cu^+ (~26%). Catalytic performance of CMZ and CM-Z deliver comparable conversion/STY at relevant WHSV, with CZ-M showing declining MeOH selectivity, underscoring that Mg must be co-introduced with Cu or Zn for stability. While MgO is often considered an inert support, these findings emphasized its role as it as a key promoter. Its interactions with Cu and Zn significantly impacted the material properties and catalytic activity in CO_2 hydrogenation to methanol. Overall, the results highlight the critical role of MgO and demonstrate that rational control of metal–support interactions *via* FSP offers a powerful alternative route for designing efficient, stable methanol synthesis catalysts.

Author contributions

The manuscript was written through contributions of all authors. L. Baumgarten worked on the conceptualization under the guidance of J.-D. Grunwaldt and E. Saraçi, on the investigation, methodology, data analysis, visualization, writing the original draft and editing. E. Kusumowidagdo, M. L. Schulte and E. N. O. A. Bauer helped with the investigation and data analysis. L. Klag supported with data interpretation and visualization. T. A. Zevaco performed N_2O titration experiments and analysis, contributing to the investigation. J. Just adjusted the beamline and supported for the acquisition and treatment of XAS data. J.-D. Grunwaldt and E. Saraçi worked on the conceptualization with L. Baumgarten, discussion on the results, visualization, manuscript writing and editing, and were responsible for project administration, resources, and supervision. All authors contributed to review & editing and have given approval to the publication of the manuscript.

Conflicts of interest

There are no conflicts to declare.

Data availability

The data supporting this article have been included as part of the supplementary information (SI). We provide additional information such as extra information on the calcination, *ex situ* characterization, synchrotron measurements and XAS data treatment and analysis.

See DOI: https://doi.org/10.1039/d6cy00469e.

Acknowledgements

The Authors gratefully acknowledge funding from the SPP2080 (358713534) by the DFG (GR3987/14-2). We thank the groups of Malte Behrens (Kiel University) and Felix Studt (KIT) for the scientific discussions on the Cu–Mg–Zn system. We thank the Balder Beamline at MAX IV Laboratory for the beamtime (proposal number 20230387). Research conducted at MAX IV, a Swedish national user facility, is supported by Vetenskapsrådet (Swedish Research Council, VR) under contract 2018-07152, Vinnova (Swedish Governmental Agency for Innovation Systems) under contract 2018-04969 and Formas under contract 2019-02496. We further acknowledge SOLEIL for provision of synchrotron radiation and their facilities (proposal number 20230169) and Dr. Stéphanie Belin for assistance at the ROCK beamline. The work at ROCK was supported by a public grant overseen by the French National Research Agency (ANR) as part of the "Investissements d'Avenir" program (reference: ANR-10-EQPX-45). Finally, J.-D. G. thanks DAPHNE4NFDI (DFG project under project number 460248799) as well as further NFDI-consortia for fruitful discussion and valuable input for implementing FAIR data principles.

References

1 B. Rego de Vasconcelos and J. M. Lavoie, *Front. Chem.*, 2019, **7**, 1–24, DOI: 10.3389/fchem.2019.00392.
2 K. F. Kalz, R. Kraehnert, M. Dvoyashkin, R. Dittmeyer, R. Glaser, U. Krewer, K. Reuter and J.-D. Grunwaldt, *ChemCatChem*, 2017, **9**, 17–29, DOI: 10.1002/cctc.201600996.
3 S. S. Tabibian and M. Sharifzadeh, *Renewable Sustainable Energy Rev.*, 2023, **179**, 113281, DOI: 10.1016/j.rser.2023.113281.
4 G. Bozzano and F. Manenti, *Prog. Energy Combust. Sci.*, 2016, **56**, 71–105, DOI: 10.1016/j.pecs.2016.06.001.
5 J. B. Hansen and P. E. Hojlund Nielsen, *Handbook of Heterogeneous Catalysis*, Wiley-VCH, 2008.
6 M. B. Fichtl, D. Schlereth, N. Jacobsen, I. Kasatkin, J. Schumann, M. Behrens, R. Schlögl and O. Hinrichsen, *Appl. Catal., A*, 2015, **502**, 262–270, DOI: 10.1016/j.apcata.2015.06.014.
7 S. Kuld, M. Thorhauge, H. Falsig, C. F. Elkjær, S. Helveg, I. Chorkendorff and J. Sehested, *Science*, 2016, **352**, 969–974.
8 J.-D. Grunwaldt, A. M. Molenbroek, N. Y. Topsøe, H. Topsøe and B. S. Clausen, *J. Catal.*, 2000, **194**, 452–460, DOI: 10.1006/jcat.2000.2930.
9 R. van den Berg, G. Prieto, G. Korpershoek, L. I. van der Wal, A. J. van Bunningen, S. Laegsgaard-Jorgensen, P. E. de Jongh and K. P. de Jong, *Nat. Commun.*, 2016, **7**, 1–7, DOI: 10.1038/ncomms13057.
10 F. Liao, Y. Huang, J. Ge, W. Zheng, K. Tedsree, P. Collier, X. Hong and S. C. Tsang, *Angew. Chem.*, 2011, **123**, 2210–2213, DOI: 10.1002/anie.201007108.
11 C. Wu, D. Cheng, M. Wang and D. Ma, *Energy Fuels*, 2021, **35**, 19012–19023, DOI: 10.1021/acs.energyfuels.1c02440.

12 P. Amann, B. Klötzer, D. Degerman, N. Köpfle, T. Götsch, P. Lömker, C. Rameshan, K. Ploner, D. Bikaljevic and H.-Y. Wang, *Science*, 2022, **376**, 603–608.

13 L. Warmuth, M. Steurer, D. Schild, A. Zimina, J.-D. Grunwaldt and S. Pitter, *ACS Appl. Mater. Interfaces*, 2024, **16**, 8813–8821, DOI: 10.1021/acsami.3c17383.

14 N.-Y. Topsøe and H. Topsøe, *Top. Catal.*, 1999, **8**, 267–270.

15 S. Natesakhawat, J. W. Lekse, J. P. Baltrus, P. R. Ohodnicki, B. H. Howard, X. Deng and C. Matranga, *ACS Catal.*, 2012, **2**, 1667–1676, DOI: 10.1021/cs300008g.

16 P. C. K. Vesborg, I. Chorkendorff, I. Knudsen, O. Balmes, J. Nerlov, A. M. Molenbroek, B. S. Clausen and S. Helveg, *J. Catal.*, 2009, **262**, 65–72, DOI: 10.1016/j.jcat.2008.11.028.

17 A. Le Valant, C. Comminges, C. Tisseraud, C. Canaff, L. Pinard and Y. Pouilloux, *J. Catal.*, 2015, **324**, 41–49, DOI: 10.1016/j.jcat.2015.01.021.

18 F. Studt, M. Behrens, E. L. Kunkes, N. Thomas, S. Zander, A. Tarasov, J. Schumann, E. Frei, J. B. Varley, F. Abild-Pedersen, J. K. Nørskov and R. Schlögl, *ChemCatChem*, 2015, **7**, 1105–1111.

19 T. Fujitani and J. Nakamura, *Catal. Lett.*, 1998, **56**, 119–124.

20 J. T. Sun, I. S. Metcalfe and M. Sahibzada, *Ind. Eng. Chem. Res.*, 1999, **38**, 3868–3872.

21 N. D. Nielsen, J. Thrane, A. D. Jensen and J. M. Christensen, *Catal. Lett.*, 2019, **150**, 1427–1433, DOI: 10.1007/s10562-019-03036-7.

22 A. Cao, Z. Wang, H. Li, A. O. Elnabawy and J. K. Nørskov, *J. Catal.*, 2021, **400**, 325–331, DOI: 10.1016/j.jcat.2021.06.020.

23 W. Liu, S. Dang, S. Cheng, Z. Zhang, X. Ding, Y. Shi, P. Ren, W. Tu and Y.-F. Han, *ACS Catal.*, 2024, **14**, 7097–7110, DOI: 10.1021/acscatal.4c00077.

24 V. Pandey, K. K. Pant and S. Upadhyayula, *React. Chem. Eng.*, 2023, **8**, 442–454, DOI: 10.1039/d2re00427e.

25 R. Dalebout, L. Barberis, G. Totarella, S. J. Turner, C. La Fontaine, F. M. F. de Groot, X. Carrier, A. M. J. van der Eerden, F. Meirer and P. E. de Jongh, *ACS Catal.*, 2022, **12**, 6628–6639, DOI: 10.1021/acscatal.1c05101.

26 L. Pandit, A. Boubnov, G. Behrendt, B. Mockenhaupt, C. Chowdhury, J. Jelic, A. L. Hansen, E. Saraçi, E. J. Ras, M. Behrens, F. Studt and J.-D. Grunwaldt, *ChemCatChem*, 2021, **13**, 4120–4132, DOI: 10.1002/cctc.202100692.

27 W. Y. Teoh, R. Amal and L. Mädler, *Nanoscale*, 2010, **2**, 1324–1347, DOI: 10.1039/c0nr00017e.

28 J. A. Dreyer, H. K. Grossmann, J. Chen, T. Grieb, B. B. Gong, P. H.-L. Sit, L. Mädler and W. Y. Teoh, *J. Catal.*, 2015, **329**, 248–261.

29 M. Høj, D. K. Pham, M. Brorson, L. Mädler, A. D. Jensen and J.-D. Grunwaldt, *Catal. Lett.*, 2013, **143**, 386–394.

30 Y. Dai, J. Ju, L. Luo, H. Jiang, Y. Hu and C. Li, *Small Methods*, 2024, **8**, 10, DOI: 10.1002/smtd.202301768.

31 C. Dimitriou, P. Psathas, M. Solakidou and Y. Deligiannakis, *Nanomaterials*, 2023, **13**, 23, DOI: 10.3390/nano13233006.

32 J. A. Kemmler, S. Pokhrel, L. Mädler, U. Weimar and N. Barsan, *Nanotechnology*, 2013, **24**, 44, DOI: 10.1088/0957-4484/24/44/442001.

33 S. Tada, K. Larmier, R. Büchel and C. Copéret, *Catal. Sci. Technol.*, 2018, **8**, 2056–2060, DOI: 10.1039/c8cy00250a.

34 R. Ahmad, M. Hellinger, M. Buchholz, H. Sezen, L. Gharnati, C. Wöll, J. Sauer, M. Döring, J.-D. Grunwaldt and U. Arnold, *Catal. Commun.*, 2014, **43**, 52–56, DOI: 10.1016/j.catcom.2013.08.020.

35 J. Zhu, D. Ciolca, L. Liu, A. Parastaev, N. Kosinov and E. J. M. Hensen, *ACS Catal.*, 2021, **11**, 4880–4892, DOI: 10.1021/acscatal.1c00131.

36 J. Yu, M. Yang, J. Zhang, Q. Ge, A. Zimina, T. Pruessmann, L. Zheng, J.-D. Grunwaldt and J. Sun, *ACS Catal.*, 2020, **10**, 14694–14706, DOI: 10.1021/acscatal.0c04371.

37 M. L. Schulte, V. Catharina Sender, L. Baumgarten, A. Beck, A. R. L. Nilayam, E. Saraçi and J.-D. Grunwaldt, *Eur. J. Inorg. Chem.*, 2024, **28**, 4, DOI: 10.1002/ejic.202400684.

38 B. Mutz, A. Gänzler, M. Nachtegaal, O. Müller, R. Frahm, W. Kleist and J.-D. Grunwaldt, *Catalysts*, 2017, **7**, 9, DOI: 10.3390/catal7090279.

39 F. Manzoni, S. Strübbe, L. Rohrbach, M. Boniface, T. Lunkenbein, R. Schoch, W. Kleist, M. Bauer and M. Zobel, *ChemCatChem*, 2025, **17**, 19, DOI: 10.1002/cctc.202500859.

40 P. Kampe, A. Wesner, P. Schuhle, F. Hess and J. Albert, *Chem*, 2023, **88**, e202300425, DOI: 10.1002/cplu.202300425.

41 M.-A. Serrer, A. Gaur, J. Jelic, S. Weber, C. Fritsch, A. H. Clark, E. Saraçi, F. Studt and J.-D. Grunwaldt, *Catal. Sci. Technol.*, 2020, **10**, 7542–7554, DOI: 10.1039/d0cy01396j.

42 A. Coelho, *J. Appl. Crystallogr.*, 2018, **51**, 210–218, DOI: 10.1107/S1600576718000183.

43 N. Brese, M. O'keeffe, B. Ramakrishna and R. Von Dreele, *J. Solid State Chem.*, 1990, **89**, 184–190.

44 R. Restori and D. Schwarzenbach, *Acta Crystallogr., Sect. B: Struct. Sci.*, 1986, **42**, 201–208.

45 H. E. Swanson, *Standard X-ray diffraction powder patterns*, US Department of Commerce, National Bureau of Standards, 1953.

46 S. Sasaki, K. Fujino and Y. Takéuchi, *Proc. Jpn. Acad., Ser. B*, 1979, **55**, 43–48.

47 H. Schulz and K. Thiemann, *Solid State Commun.*, 1979, **32**, 783–785.

48 K. Klementiev, K. Norén, S. Carlson, K. S. Clauss and I. Persson, The BALDER beamline at the MAX IV laboratory, *J. Phys.: Conf. Ser.*, 2016, **712**, 012023.

49 V. Briois, C. La Fontaine, S. Belin, L. Barthe, T. Moreno, V. Pinty, A. Carcy, R. Girardot and E. Fonda, ROCK: the new Quick-EXAFS beamline at SOLEIL, *J. Phys.: Conf. Ser.*, 2016, **712**, 012149.

50 C. La Fontaine, S. Belin, L. Barthe, O. Roudenko and V. Briois, *Synchrotron Radiat. News*, 2020, **33**, 20–25.

51 G. Landrot and E. Fonda, *J. Synchrotron Radiat.*, 2025, **32**, 1085–1094, DOI: 10.1107/S1600577525003923.

52 B. Ravel and M. Newville, *J. Synchrotron Radiat.*, 2005, **12**, 537–541.

53 M. A. Serrer, M. Stehle, M. L. Schulte, H. Besser, W. Pfleging, E. Saraçi and J.-D. Grunwaldt, *ChemCatChem*, 2021, **13**, 3010–3020, DOI: 10.1002/cctc.202100490.

54 M.-F. Luo, P. Fang, M. He and Y.-L. Xie, *J. Mol. Catal. A: Chem.*, 2005, **239**, 243–248, DOI: 10.1016/j.molcata.2005.06.029.

55 W.-P. Dow, Y.-P. Wang and T.-J. Huang, *Appl. Catal., A*, 2000, **190**, 25–34.

56 Z. Huang, F. Cui, J. Xue, J. Zuo, J. Chen and C. Xia, *Catal. Today*, 2012, **183**, 42–51, DOI: 10.1016/j.cattod.2011.08.038.

57 X. Yang, H. Chen, Q. Meng, H. Zheng, Y. Zhu and Y. W. Li, *Catal. Sci. Technol.*, 2017, **7**, 5625–5634, DOI: 10.1039/c7cy01284e.

58 G. Fierro, M. L. Jacono, M. Inversi, P. Porta, F. Cioci and R. Lavecchia, *Appl. Catal., A*, 1996, **137**, 327–348.

59 Z. Lin, D. Han and S. Li, *J. Therm. Anal. Calorim.*, 2012, **107**, 471–475.

60 I. Youssef, S. Sall, T. Dintzer, S. Labidi and C. Petit, *Am. J. Anal. Chem.*, 2019, **10**, 153–170.

61 E. Rodríguez-Jara, M. Cavallo, R. Nakazato, M. Quintelier, K. Matsumoto, J. Hadermann, J. Mosa, F. Bonino, K. Tadanaga and M. Aparicio, *Open Ceram.*, 2025, **21**, 100733.

62 T. Arii and A. Kishi, *Thermochim. Acta*, 2003, **400**, 175–185.

63 Y. Jiang, H. Chen, X. Mu and Z. He, In Thermal decomposition of magnesium acetate in nitrogen, *J. Phys.: Conf. Ser.*, 2020, **1653**, 012057.

64 R. M. Laine, J. Marchal, H. Sun and X. Q. Pan, *Adv. Mater.*, 2005, **17**, 830–833.

65 B. Maack and N. Nilius, *Thin Solid Films*, 2018, **651**, 24–30, DOI: 10.1016/j.tsf.2018.02.007.

66 R. A. Lewis, *Hawley's condensed chemical dictionary*, 16 edn, John Wiley & Sons, 2016.

67 D. F. Anthrop and A. W. Searcy, *J. Phys. Chem.*, 1964, **68**, 2335–2342.

68 K. M. S. Koumoto and H. Yanagida, *J. Ceram. Soc. Jpn.*, 1980, **88**, 217–227.

69 C. Alexander, J. Ogden and A. Levy, *J. Chem. Phys.*, 1963, **39**, 3057–3060.

70 T. Samerjai, C. Liewhiran and S. Phanichphant, Synthesis of MgO/ZnO nanocomposites by flame spray pyrolysis, in *Advanced Materials and Nanotechnology*, AIP Conf. Proc Dunedin, New Zealand, 2009, vol. 1151, pp. 17–20.

71 H. Li, H. Tian, S. Chen, Z. Sun, T. Liu, R. Liu, S. Assabumrungrat, J. Saupsor, R. Mu and C. Pei, *Appl. Catal., B*, 2020, **276**, 119052.

72 Y. Y. Li, M. M. Wan, X. D. Sun, J. Zhou, Y. Wang and J. H. Zhu, *J. Mater. Chem. A*, 2015, **3**, 18535–18545.

73 J. W. Kim, H. S. Kang, J. H. Kim, S. Y. Lee, J.-K. Lee and M. Nastasi, *J. Appl. Phys.*, 2006, **100**, 3, DOI: 10.1063/1.2219153.

74 N. Pasupulety, G. L. Rempel and F. T. T. Ng, *Appl. Catal., A*, 2015, **489**, 77–85, DOI: 10.1016/j.apcata.2014.10.015.

75 S. Chawla, K. Jayanthi, H. Chander, D. Haranath, S. K. Halder and M. Kar, *J. Alloys Compd.*, 2008, **459**, 457–460, DOI: 10.1016/j.jallcom.2007.04.303.

76 M. A. Dar, Y. S. Kim, W. B. Kim, J. M. Sohn and H. S. Shin, *Appl. Surf. Sci.*, 2008, **254**, 7477–7481, DOI: 10.1016/j.apsusc.2008.06.004.

77 W. Wei, *J. Mater. Sci. Appl.*, 2016, **5**, 1, DOI: 10.11648/j.ijmsa.20160501.13.

78 M. Wu, Y. Fu, W. Zhan, Y. Guo, Y. Guo, Y. Wang and G. Lu, *Catalysts*, 2017, **7**, 5.

79 A. Kaleva, T. Tassaing, V. Saarimaa, G. Le Bourdon, P. Väisänen, A. Markkula and E. Levänen, *Corros. Sci.*, 2020, **174**, 108850, DOI: 10.1016/j.corsci.2020.108850.

80 J.-M. Nunzi, H. Ftouhi, Z. El Jouad, M. Jbilou, M. Diani, M. Addou, R. Bennacer, M. El Ganaoui and M. El Jouad, *Eur. Phys. J.:Appl. Phys.*, 2019, **87**, 10301, DOI: 10.1051/epjap/2019190111.

81 W.-B. C. Cai and D. A. Scherson, *J. Electrochem. Soc.*, 2003, **150**, 217–223, DOI: 10.1149/1.1563651.

82 A. Rumyantseva, S. Kostcheev, P.-M. Adam, S. V. Gaponenko, S. V. Vaschenko, O. S. Kulakovich, A. A. Ramanenka, D. V. Guzatov, D. Korbutyak and V. Dzhagan, *ACS Nano*, 2013, **7**, 3420–3426.

83 X. Zhu, H.-Z. Wu, D.-J. Qiu, Z. Yuan, G. Jin, J. Kong and W. Shen, *Opt. Commun.*, 2010, **283**, 2695–2699, DOI: 10.1016/j.optcom.2010.03.006.

84 H. J. Fan, R. Scholz, F. M. Kolb, M. Zacharias, U. Gösele, F. Heyroth, C. Eisenschmidt, T. Hempel and J. Christen, *Appl. Phys. A: Mater. Sci. Process.*, 2004, **79**, 1895–1900, DOI: 10.1007/s00339-004-2933-2.

85 J. S. Lee, S. H. Han, H. G. Kim, K. H. Lee and Y. G. Kim, *Korean J. Chem. Eng.*, 2000, **17**, 332–336.

86 F. Chen, W. Gao, K. Wang, C. Wang, X. Wu, N. Liu, X. Guo, Y. He, P. Zhang, G. Yang and N. Tsubaki, *Fuel*, 2022, **315**, 123272, DOI: 10.1016/j.fuel.2022.123272.

87 L. D. Ernst, D. Guse, N. Schmidt-Meinzer, M. Kind and I. Krossing, *Z. Anorg. Allg. Chem.*, 2026, **652**, 7, DOI: 10.1002/zaac.202500235.

88 T. Guo, Q. Guo, S. Li, Y. Hu, S. Yun and Y. Qian, *J. Catal.*, 2022, **407**, 312–321, DOI: 10.1016/j.jcat.2022.01.035.

89 G. Fierro, M. L. Jacono, M. Inversi, P. Porta, F. Cioci and R. Lavecchia, *Appl. Catal., A*, 1996, **137**, 327–348.

90 G. Fierro, M. Lojacono, M. Inversi, P. Porta, R. Lavecchia and F. Cioci, *J. Catal.*, 1994, **148**, 709–721.

91 S. K. Sharma, T. S. Khan, R. K. Singha, B. Paul, M. K. Poddar, T. Sasaki, A. Bordoloi, C. Samanta, S. Gupta and R. Bal, *Appl. Catal., A*, 2021, **623**, 118239, DOI: 10.1016/j.apcata.2021.118239.

92 M. Jabłońska, B. Wolkenar, A. M. Beale, S. Pischinger and R. Palkovits, *Catal. Commun.*, 2018, **110**, 5–9.

